



## Quasi-steady front in quench subcooled-jet impingement boiling: Experiment and analysis



Sang Gun Lee<sup>a</sup>, Massoud Kaviany<sup>b</sup>, Charn-Jung Kim<sup>a</sup>, Jungho Lee<sup>c,\*</sup>

<sup>a</sup> School of Mechanical and Aerospace Engineering, Seoul National University, Seoul 08826, South Korea

<sup>b</sup> Department of Mechanical Engineering, University of Michigan, Ann Arbor, MI 48109, USA

<sup>c</sup> Department of Energy Conversion Systems, Korea Institute of Machinery & Materials, Daejeon 34103, South Korea

### ARTICLE INFO

#### Article history:

Received 10 January 2017

Received in revised form 19 May 2017

Accepted 21 May 2017

#### Keywords:

Boiling heat transfer

Water jet impingement

Surface thermal characteristics

Inverse heat conduction

Quasi-steady regime

### ABSTRACT

Boiling heat transfer of subcooled water jet impingement on highly superheated plate is investigated with heat transfer analysis and high-definition flow visualization. The stainless steel plate initially heated up to 900 °C by an induction heating is quenched with the water temperature of 15 °C. The surface temperature and heat flux are estimated by solving 2-D inverse heat conduction problem. The temporal visualization during quench subcooled-jet impingement boiling is synchronized with the heat transfer measurement in the corresponding surface temperature and heat flux. Spread of the subcooled jet over the horizontal plate shows a quasi-steady regime where the wetting front spreads linearly with time. The time for onset of the quasi-steady regime can be explained by a quasi-steady time. The front separates the single-phase/collapsed-bubble region from the outside region which is dry if not for the impinging droplets ejected from the front. As the front expands, the surface experiences a sequence of single-phase, collapsed-bubble, wetting front evaporation and ejected-droplet evaporation cooling. The fraction of water ejected from the front increases linearly with time (reaches over 10%) and is also predicted.

© 2017 Elsevier Ltd. All rights reserved.

### 1. Introduction

In material processing, the quenching processes strongly control the phase transformation, grain size distribution and thermal stresses of metallic work pieces. Water jet impingement has been widely used for its rapid and intensive cooling capacity [1–5]. The surface morphology, structure and composition of the quenched steel are also characterized by the initial heating and then the cooling rate during quenching process. However the fundamental studies of this cooling process are rather sparse due to complexity of its transient, heterogeneous boiling modes, in particular for subcooled jets. The boiling heat transfer is also affected by the dimensions and thermal properties of the quenched material (metallic). So, a thorough understanding of boiling heat transfer, including the hydrodynamic of the jet impingement, is required for predicting the characteristics and the qualitative improvement in material. Here we aim at providing further insights into the jet quench boiling and Fig. 1 gives a schematic of the subcooled circular free-surface jet flowing over a highly superheated surface, showing three different regions, namely the wet, wetting front, and dry region. Furthermore, at the stagnation point shortly after

cooling commences, and under high local heat flux (cooling rate), evaporation is suppressed, and single-phase convection cooling continues there. At larger radial locations, the surface temperature is in high and due to the subcooled jet, the region of collapsed-bubble boiling prevails. Further outward, the dry region is reached with an active droplet spouting evaporation front. The otherwise dry region is not cooled by landing of these droplets which evaporate with intensity depending on the local landing site surface superheat.

A review of prior experimental investigations into the characteristics of jet impingement quenching is given by Wolf et al. [6], covering the hydrodynamics of the jet flow, various boiling regimes, and key jet-surface parameters. But, few experiments regarding rapid cooling on a high-temperature surface over 500 °C were investigated due to complicated coupled boiling heat transfer in highly unsteady cooling. The visual observation reveals formation of “dark zone” (contrast by glowing high superheat region) beneath the jet (Karwa et al. [7]) with the surface temperature there under 500 °C with the peripheral boundary of this zone called the wetting front. The liquid deflection was observed outside of wetting front due to surface tension and shear forces. These splashed droplet velocity is governed by jet velocity. Hall et al. [8] and Ishigai et al. [9] reported that film boiling was not observed in the stagnation region with highly subcooled jet, even though an

\* Corresponding author.

E-mail address: [jungho@kimm.re.kr](mailto:jungho@kimm.re.kr) (J. Lee).



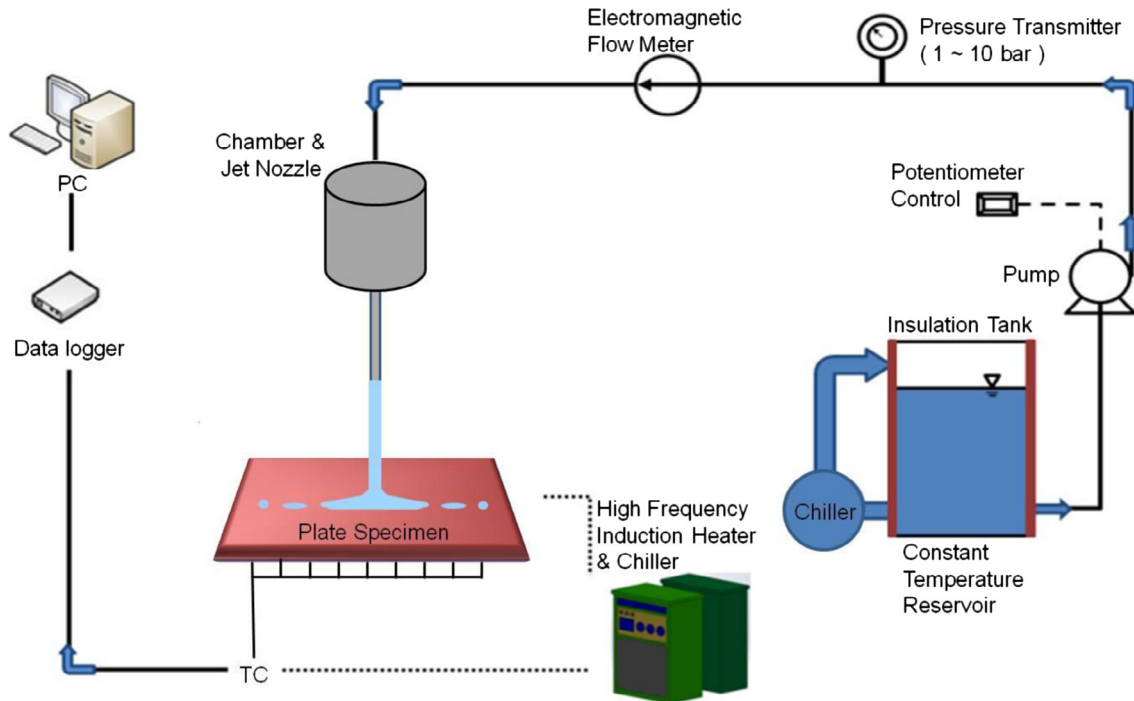


Fig. 2. Schematic of the jet quench boiling experiment and its components.

ered by a pump (CRN 1-15, Grundfos) which has nearly total head of 100 m. The water flow rate was directly measured by an electromagnetic flowmeter (GF630A/LF600, Toshiba). During the experiments, the water flow rate was consistently kept constant as determined from an electromagnetic flowmeter connected in the flow loop. The water chamber with jet nozzle is mounted 100 mm above the flat plate center with axisymmetric circular nozzle. The center of the nozzle is carefully aligned to the center of the heated flat plate with a laser pointed guide. The distance between the nozzle and the surface of the heated surface is fixed at 100 mm. The inner diameter of the nozzle is 3 mm and its length is 100 mm. The water flow rate is  $0.14 \text{ m}^3/\text{h}$ , corresponding to Reynolds number ( $Re_D$ ) of 15,000. The measurement uncertainty is within 0.7%, for the volumetric flow rate measurement.

The test flat plate and its embedded thermocouples used as the high-temperature heat flux gauge are shown in Fig. 3. The test assembly consists of flat plate, induction heating system, porous ceramic insulators and the thermocouples. An image of the heat flux gauge is shown in Fig. 3(a), and the plate is made of stainless-steel ANSI 304 which avoids phase-transformation heat generation encountered in most of carbon steels. The 304 stainless-steel is well known for its chemical inertness at elevated temperature and does not go through solid–solid phase transformation that can exert noticeable amount of heat and distract temperature reading during water quenching process. The flat plate is rectangular, length 300 mm, width 200 mm and thickness of 20 mm, with twenty-two  $1 \pm 0.1$  mm diameter holes drilled accurately through electric discharge machining (EDM). 22 K-type thermocouples (KMTXL-040G-6, OMEGA) with 1 mm thick are installed inside the test flat plate as shown in Fig. 3(b). Nineteen holes have depth of 19 mm and are radially 15 mm apart. Three holes have depth of 5, 10 and 15 mm respectively and are located near the plate center. The thermocouples are placed in these holes and precisely spot welded. A calibration on thermocouples is carefully performed with platinum resistance thermometer and the uncertainty of the thermocouples is found to be within  $0.1 \text{ }^\circ\text{C}$ . Temperature is measured and recorded with high-speed data

acquisition system (EX1032A, VTI Instruments Co.) with sampling rate of 10 data/s. The side and bottom of the plate are thermally insulated with porous ceramic insulators.

Induction heating is used to heat the plate up to  $900 \text{ }^\circ\text{C}$  above austenite temperature. Induction heating suited for noncontact heating is applied using rectangular-shaped coil specially manufactured for uniform heating. The rectangular-shaped coil unit with tube diameter is 9.4 mm is placed above the plate. When high-frequency of 19 kHz current is applied to the coil, eddy current is generated on the surface of the plate by Faraday's law. So the joule heating is the product of electrical resistance of the material and square of the induced current. During the induction heating process, as the eddy current generation is uniformly distributed in the plate, and its temperature maintains at  $1000 \text{ }^\circ\text{C}$  within  $5 \text{ }^\circ\text{C}$  across the plate. By using the induction heating method, the plate electrically heated up to  $1000 \text{ }^\circ\text{C}$  within 20 min. An ultra-high-definition (UHD) video camera is used to visualize the complex boiling phenomena on the heated flat plate during the water jet quenching. The UHD camera is also synchronized to the data acquisition system which is to measure temperatures inside the flat plate.

## 2.2. Inverse heat conduction analysis

To quantify the boiling heat transfer characteristics, the surface thermal characteristics such as temperature and heat flux are required and without disturbing the jet flow on the surface, we adopt the numerical method of estimating the local heat transfer characteristics using the plate internal temperature distribution (from thermocouples). The inverse heat conduction method of Twomey [19] and Beck et al. [20] is used and the flow chart is shown in Fig. 4 for obtaining the axisymmetric temperature distribution. The measured data is converted and imported into the calculation nodes of axisymmetric IHCP domain with the initial temperature known. The unknown temperature at each position is calculated by interpolation. The unknown boundary condition (heat flux) is initially assumed and the temperature distribution is updated using the calculated temperature by the direct problem.

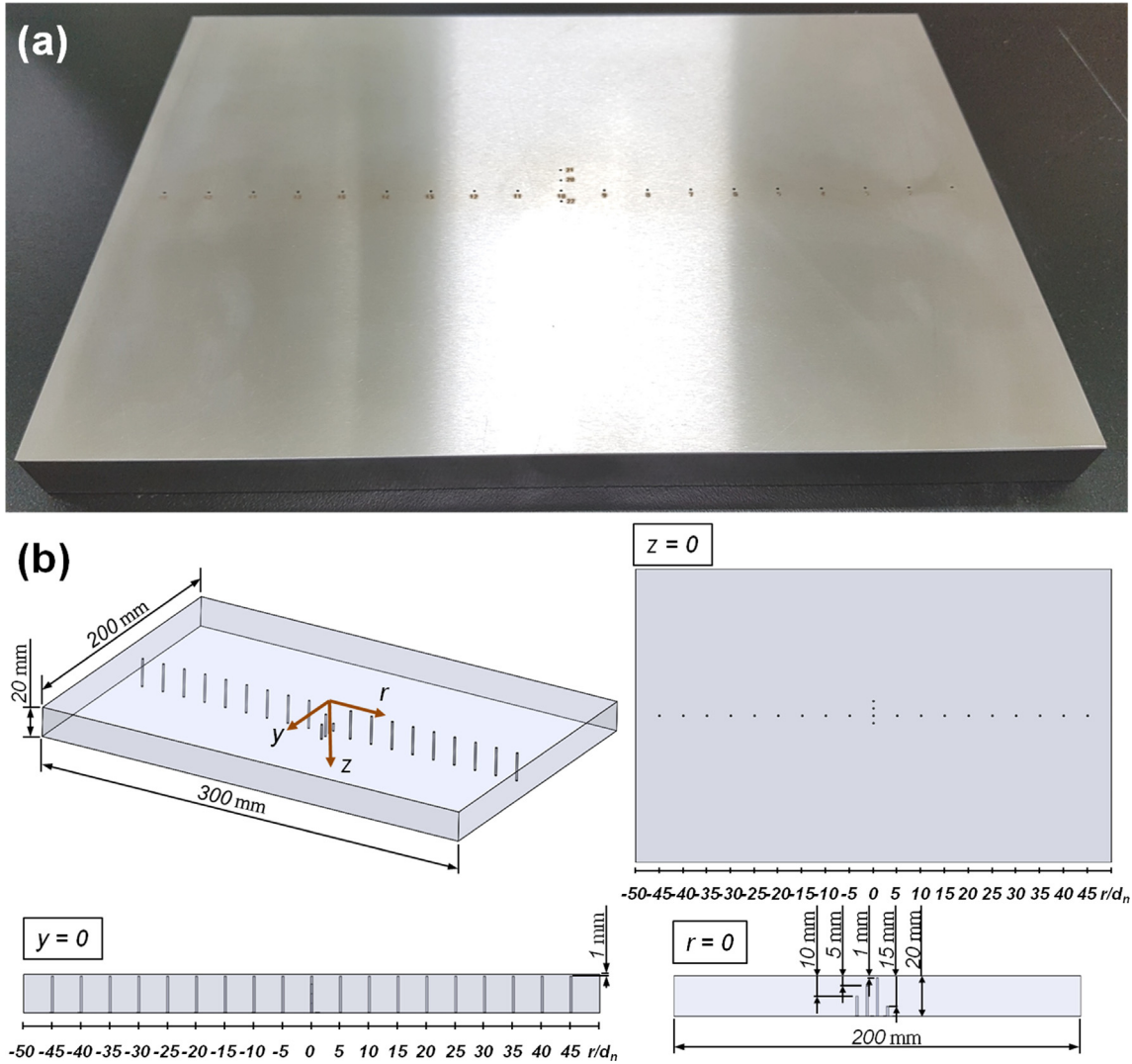


Fig. 3. (a) Image of the stainless-steel plate and the locations of the thermocouples, (b) Schematic of the thermocouple-holes for measuring temperature.

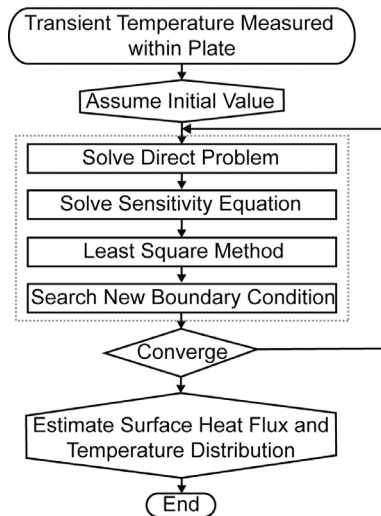


Fig. 4. Flow chart of axisymmetric inverse heat conduction for determining the plate transient surface temperature and heat flux distributions based on internally measured transient temperatures.

In direct problem, the information of assumed boundary condition feeds into the temperature distribution. Because the IHCP is extremely sensitive to the measurement errors, the concept of sensitivity coefficient ( $\zeta$ ) is adopted to improve the experimental design. The sensitivity coefficient is defined as the first derivative of a dependent variable, such as the temperature, with respect to the unknown heat flux. The mathematic formulation of the sensitivity coefficient is expressed as

$$\delta T_{k,i}(r, z, t) = \delta T_{k,i}^*(r, z, t) + \frac{\partial T_{k,i}^*(r, z, t)}{\partial q_k} \Big|_{q_k=q_k^*} (q_k - q_k^*) + \dots \quad (1)$$

$$\approx \delta T_{k,i}^*(r, z, t) + \zeta_{k,i}(q_k - q_k^*)$$

where \* indicates former time iteration and subscripts  $k$  and  $i$  present the time and position. The calculated data is applied to sum of the squared functions ( $\Sigma$ ) to search for an optimal boundary condition by minimizing the  $\Sigma$ . The difference between measured and calculated temperature is

$$\Sigma = \sum_{i=1}^N [T_{k,i}^m(r, z, t) - T_{k,i}^c(r, z, t)] \quad (2)$$

where  $N$  is the total number of measurement points. The comparison of measured temperature ( $T^m$ ) at 1 mm from the surface and

calculated temperature ( $T^c$ ) at the surface are shown in Fig. 5(a)–(b). The dotted lines represent the measured temperature and the solid lines denote the calculated temperature from the IHCP. The graphs show good agreement, with a maximum error less than 4%.

### 3. Results and discussion

#### 3.1. Flow visualization and cooling regions

Fig. 6 shows sequence of images of jet quench boiling and during early stage (short elapsed time), Fig. 6(a)–(d), the cooled region (black) grows as a circular around the stagnation point. There is also droplet ejection which is ejected at the wetting front. In Fig. 6(d) there are three distinct regions, namely, wetted, wetting front, and dry region and these are also shown in Fig. 7(a). The covered the black spot area and its inner portion is single-phase convection while the outer portion is subcooled (collapsed bubble)

boiling. In the dry region, the ejected droplets land (impinge) and evaporate under high surface superheat (Leidenfrost effect). The droplet hovers over the surface without physical contact and quickly ejected to outside of the specimen. The wetting front region is defined as the intermediate part between the wetted region and dry region. With increase in elapsed time in Fig. 6(e)–(i), the radius of black region grows but the front speed decreases due to the area expansion and there appears to be a hydraulic jump is formed as seen in Fig. 7(b). This radius of hydraulic jump depends on the initial jet flow velocity and the surface roughness which occurs when water flow is hindered. As shown in the Fig. 6(e)–(i), the wetting front region becomes larger with violent boiling. But, it should be noted that the surface of wetting front region remained unwetted like as the film boiling in pool boiling.

Above-mentioned visualization results are well synchronized with a quantitative analysis of IHCP result. Fig. 5(b) shows the transient temperature distribution at various radial locations along elapsed time. The slope of each graph closely associates with the

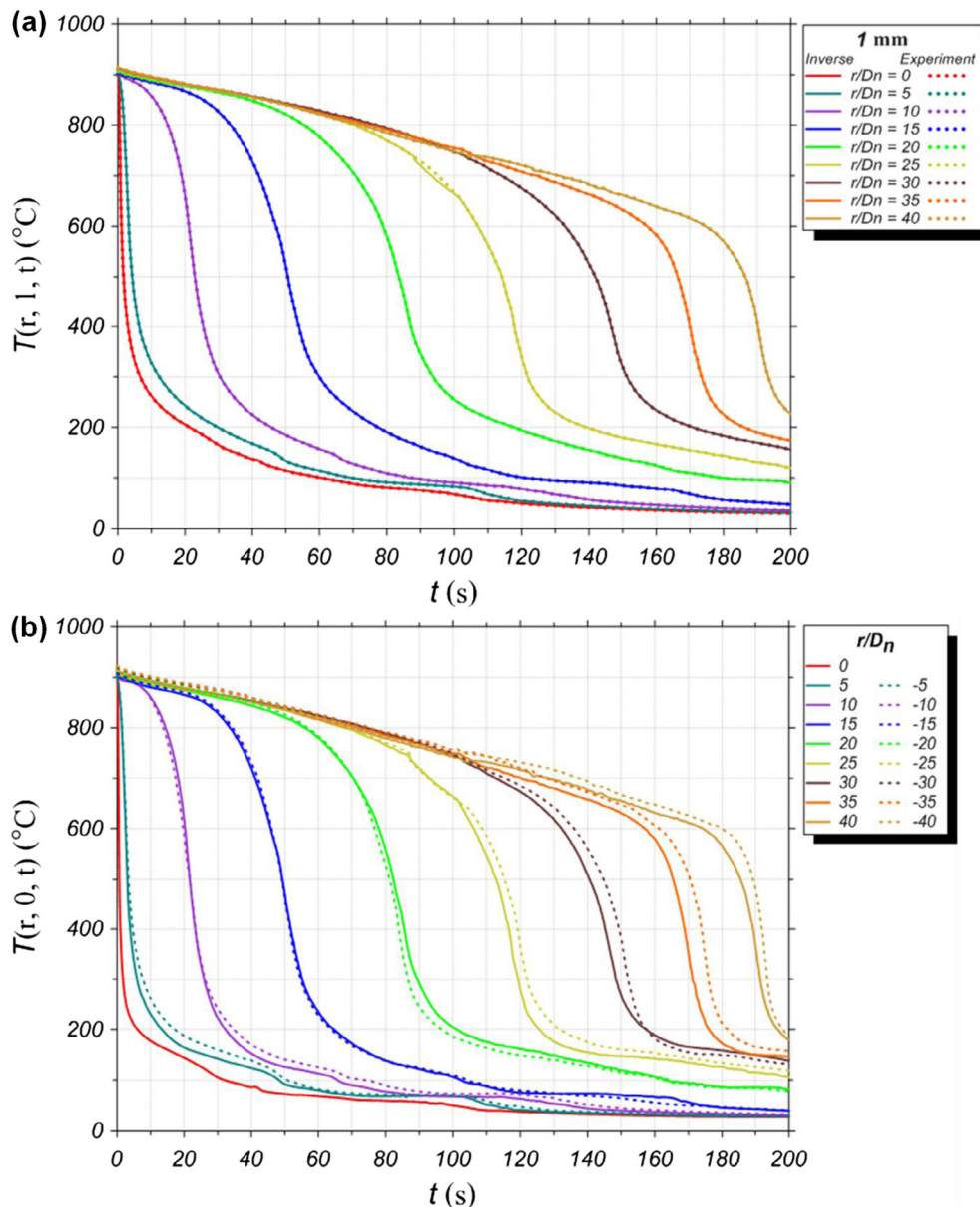
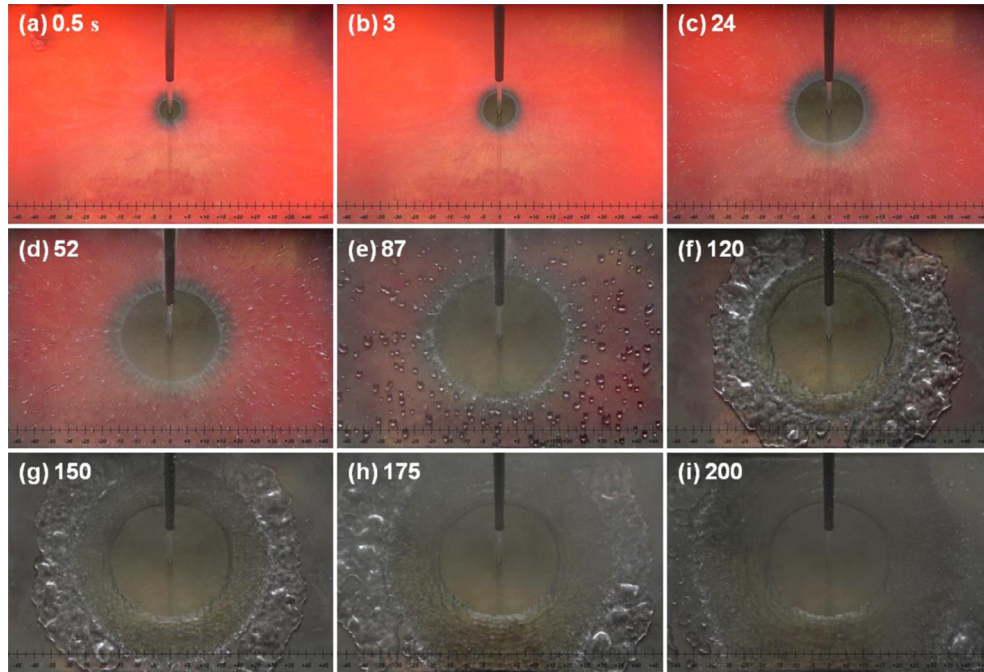
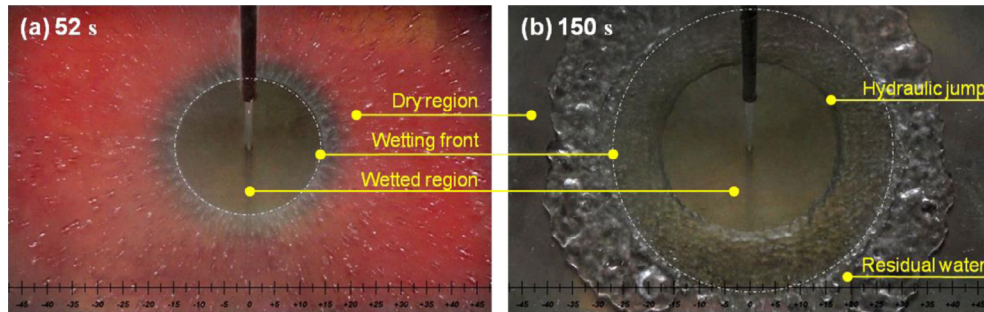


Fig. 5. Comparison between the measured and predicted (inverse heat conduction) plate temperature distributions at several radial locations: (a) 1 mm below surface and (b) at surface.



**Fig. 6.** Snapshot images of spreading jet, for several elapsed times, showing the wetting front, liquid eject (droplets), and eventual cooling of the plate (fading out red color). The progressively increasing central single-phase and the collapsed-bubble regions are also observed. The radial location is shown at the bottom of each snapshot. (For interpretation of the references to colour in this figure legend, the reader is referred to the web version of this article.)



**Fig. 7.** Snapshot image comparison at two elapsed times, with marking of the various regions. (a) Plate has significant superheat, and (b) plate is significantly cooled with large subcooled single-phase inner region. The spread of the wetting front is linear with time. The fraction liquid eject from the front remains constant with time, but the front perimeter increases so the droplet are more spread.

local boiling regime at specific time. The temperature distribution of  $r/D_n = 0$  shows rapid gradient in early time ( $<0.8$  s), and, after that, its slope becomes gradual and almost flat after 60 s. Since the coolant directly impinges on the stagnation point, the surface is wetted in very short time and the nucleate boiling immediately occurs [8,9]. Therefore, the film boiling regime could not be observed in the graph of  $r/D_n = 0, \pm 5$ . The nucleate boiling results in the sharp temperature drop but disappears going through the transition boiling. After that, the single-phase convection accompanying gradual temperature drop is followed. Comparing to the slopes of  $r/D_n = 0$  and  $\pm 5$ , the temperature profile of outside zone ( $\pm 10 \leq r/D_n \leq \pm 40$ ) shows three steps: a slow grade in early stage, a steep grade in middle stage and a modest gradient until final stage. Each step of slope is categorized as a film boiling, a nucleate boiling and single-phase convection, respectively.

The specific boiling regimes are specified in more detail with the local heat flux distribution at various radial locations against the local surface superheat of Fig. 8. The heat flux distribution shows almost zero at beginning stage in the Fig. 8(a). But Karwa et al. [7] and Akmal et al. [21] suggested that the time response

of the thermocouple can lead the additional delay on the time required to reach the maximum heat flux ( $q_{\max}$ ). Considering the limitation of measurement technique, we can assume that the  $q_{\max}$  of the  $r/D_n = 0$  appears almost at the initial jet impingement quench as marked with dotted red line. Whereas one of  $q_{\max}$  appears in Fig. 8(a), the Fig. 8(b) and (c) show two and three of peaks, separately. Each of peak value is originated from the distinct boiling heat transfer regime. The sole peak in radial position of  $r/D_n = 0, \pm 5$  in Fig. 8(a) shows high value of  $q_{\max}$  that reaches 6.4 and 3.2 MW/m<sup>2</sup>. The temperature where the nucleate boiling occurs relates with the value of  $q_{\max}$ . These high values come from the nucleate boiling occurs in short time right after jet impingement. On the other hand, the first peak in radial position of  $r/D_n = \pm 10, \pm 15$  and  $\pm 20$  is originated from the air and droplet cooling. When the radius of wetting area is smaller than each of radial position, the surface is unwetted and the surface temperature is gradually decrease until 850 °C as shown in Fig. 5(b). After the surface wetting, the nucleate boiling regime starts with heat flux increasing and shows the second maximum peak with  $q_{\max}$ . The value of  $q_{\max}$  of Fig. 8(b) is smaller than that in Fig. 8(a) due to

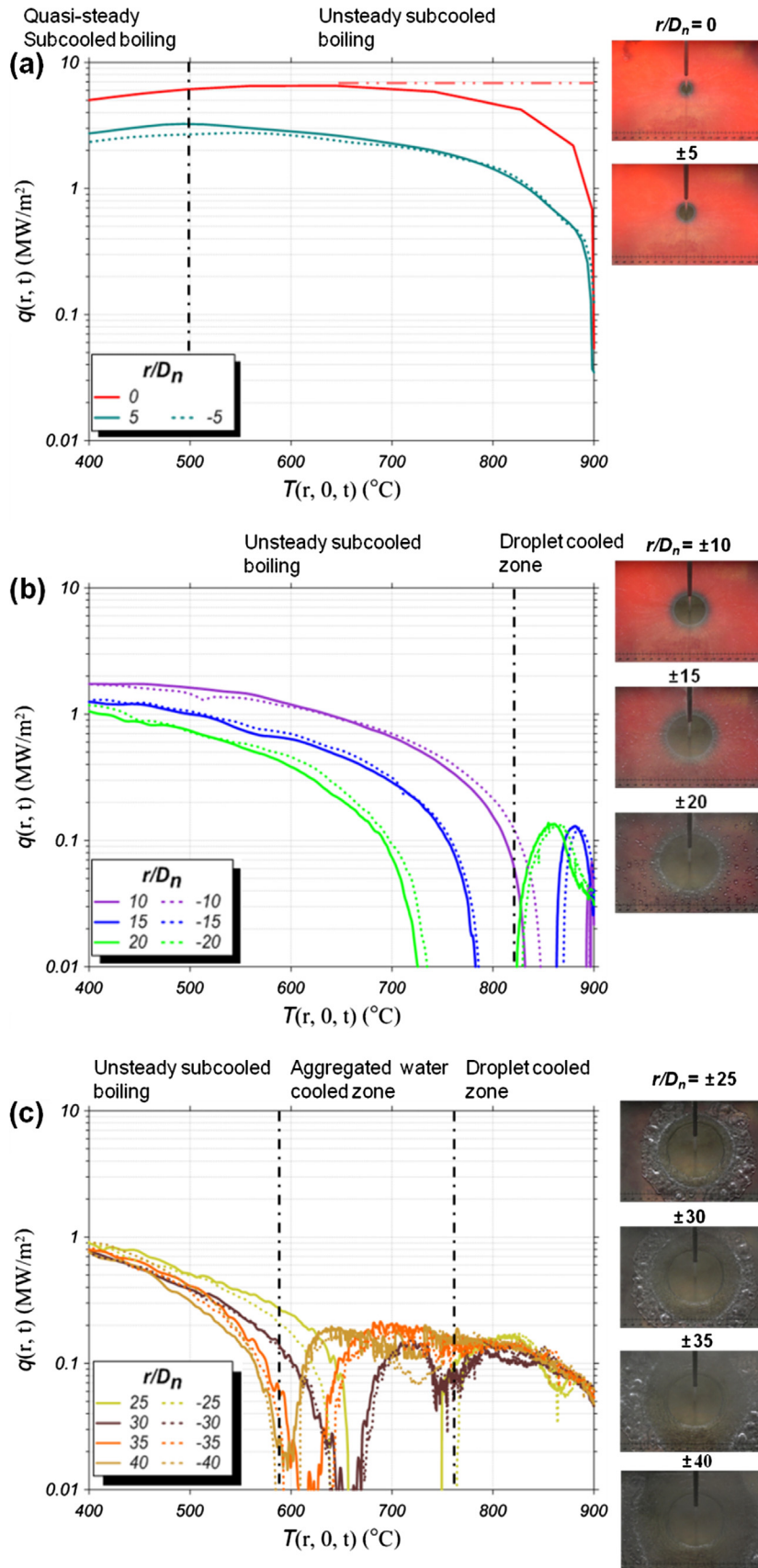


**Fig. 8.** Variations of the transient local surface flux with respect to local surface superheat at various radial locations: (a) inner, (b) middle, and (c) outer regions. Note that two set of data are shown for each radial location (one each side) to confirm presence of symmetry. The inner region is least affected by cooling with the ejected droplets, so has experiences rather steady cooling, while the outer region is substantially cooled by droplets before the front arrives.

the lower starting temperature of nucleate boiling. The more outer radial position of  $r/D_n = \pm 25, \pm 30, \pm 35$  and  $\pm 40$  shows three bends of curves. Like as Fig. 8(b), the first curve located in right side comes from the air and droplet cooling, and the third curve in left side presents the nucleate and transition boiling regime. The second curve in middle part is caused by the residual water at wetting front region. Fig. 9 shows local heat flux at  $r/D_n = \pm 30, \pm 40$  with respect to the surface temperature and elapsed time, separately, shows the boiling phenomenon of second curve more specifically. The starting temperature and time of second curve of  $r/D_n = \pm 30$  in Fig. 9(a) is relatively higher than that of  $r/D_n = \pm 40$  in Fig. 9(c). It is due to the outer side is cooled in more time with droplet cooling. After starting residual water cooling, Fig. 9(b) is for larger elapsed time compared to Fig. 9(d). The residual water with stagnant flow motion causes the film boiling phenomenon in pool boiling and the magnitude of heat flux in wetting front region is almost same with the droplet cooling in wetting region. This confirms nucleate boiling does not occur at the wetting front.

3.2. Quasi-steady regime

Figs. 10 and 11 show the synchronization of boiling visualization with the surface temperature, heat flux and heat transfer coefficient along the wetting radius with specific time. The orange

colored vertical means the position of  $q_{max}$  calculated by IHCP at specific time. At the start of quenching in Fig. 10(a), the  $q_{max}$  and maximum heat transfer coefficient locates at the stagnation point. And the starting temperature of nucleate boiling is almost same with the initial temperature of 900 °C. It confirms again that the film boiling does not occur at the stagnation point. At the wetting radius of  $R_{do}/D_n = \pm 5$  in Fig. 10(b), the temperature at the stagnation point decreases near 250 °C and shows sharp gradient along radial position. The nucleate boiling site with  $q_{max}$  positions at the inner of wetting radius has relatively low value than that of Fig. 10(a). After that, the  $q_{max}$  position of Fig. 10(c) and (d) shows almost accords with the boundary of wetted region. This result indicates that the nucleate boiling occurs in very early time where the jet flow is directly impinged. But after the short time, the surface wetting is the key of distinguishing the position of nucleate boiling site. This tendency is continuously observed in more elapsed time of Fig. 11. In Fig. 11(a)–(c), the position of  $q_{max}$  is completely identical with the wetting radius. But at the outer radial position of  $R_{do}/D_n = \pm 35$  in Fig. 11(d), the nucleate boiling with  $q_{max}$  locates slightly out boundary of wetted region. It can be regarded as due to the long duration of residual water cooling. Moreover, it is also confirmed again that the nucleate boiling temperature which is overlapped with vertical line decreases and the magnitude of  $q_{max}$  decreases with the same rate. However the

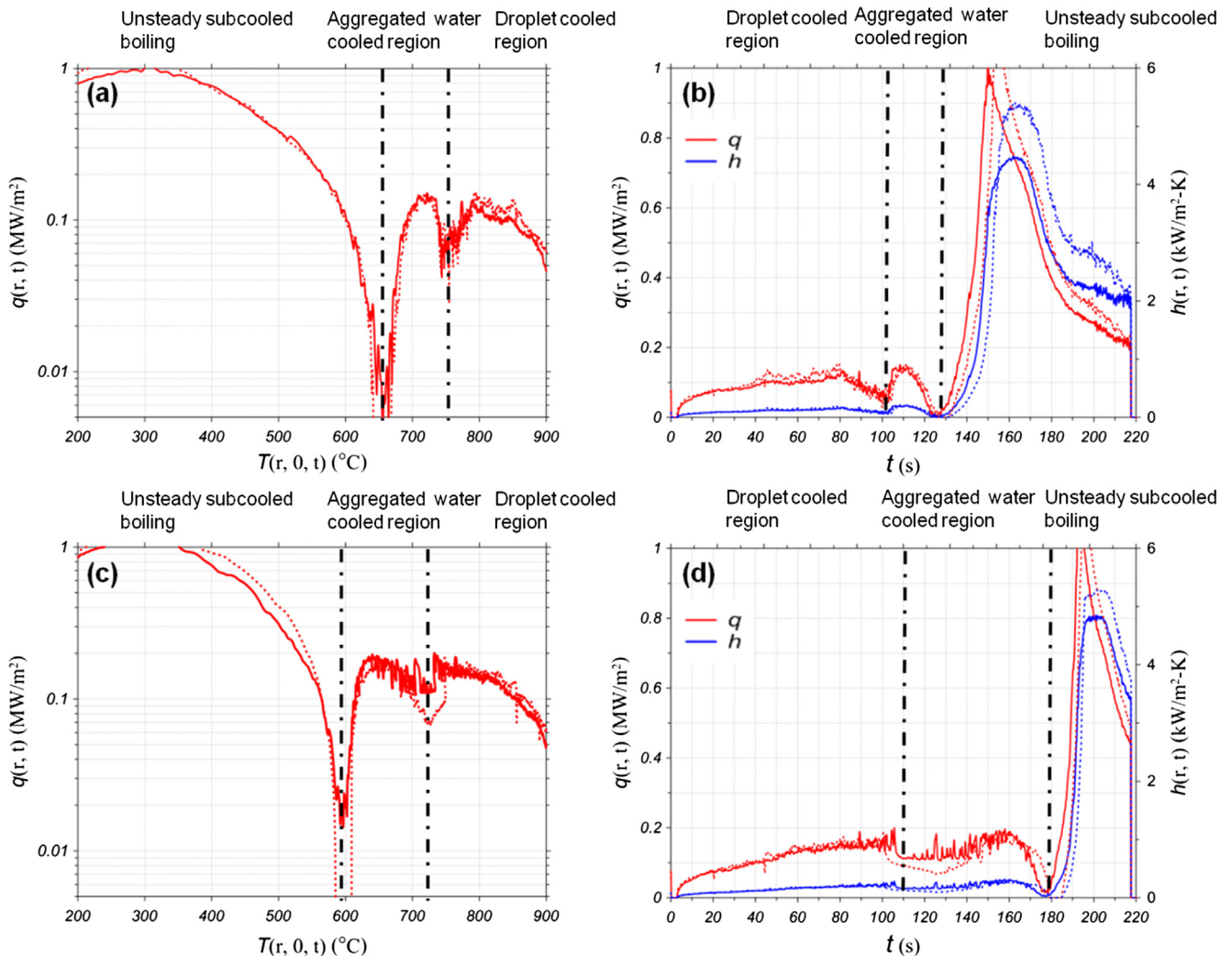


Fig. 9. (a) Variations of local surface heat flux distribution with respect to the local surface superheat and (b) variations of the local surface heat flux and heat transfer coefficient with respect to time, at locations  $r/D_n = \pm 30$ . (c) and (d), same but for  $r/D_n = \pm 40$ . Various cooling regime encountered are also shown.

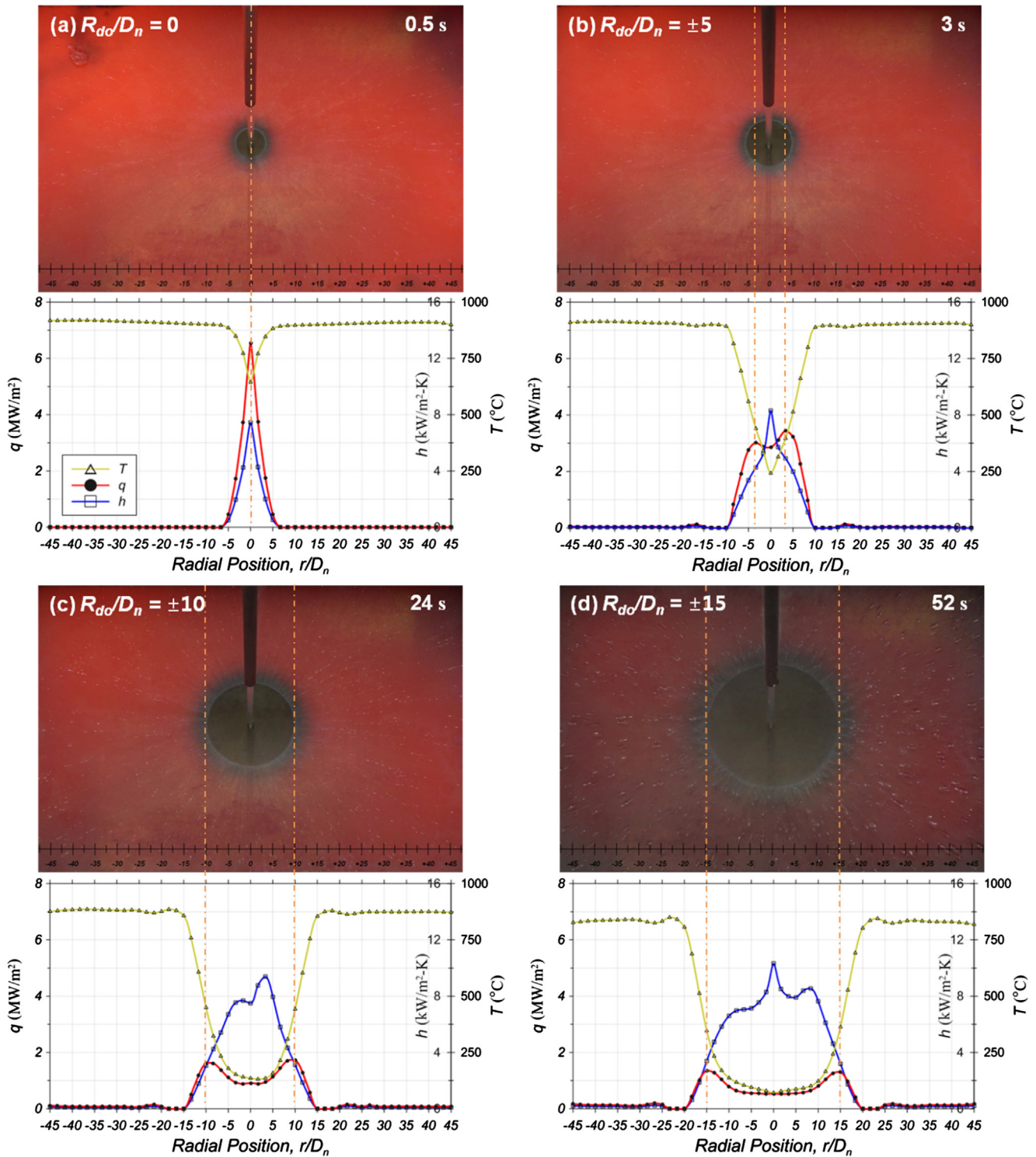


Fig. 10. Snapshot image combined with the radial distributions of the surface heat flux and heat transfer coefficient at wetting front radii  $R_{d0}/D_n$  (a)  $\pm 0$ , (b)  $\pm 5$ , (c)  $\pm 10$ , and (d)  $\pm 15$ . The elapsed time is chosen accordingly to reveal the regimes.

decrease of  $q_{\max}$  over time becomes rapidly smaller after the specific time of 24 s as shown in Fig. 10(c).

From above-results, it can be seen that the distinct tendency comes to existence from the comparison of boiling visualization with thermal distribution data by IHCP. After a specific time, the position of  $q_{\max}$  is approximately identical to that of wetting radius. We assume that not only the temperature distribution of surface but also the inner temperature of specimen can associate

with the boiling phenomenon. Fig. 12 shows the sequence of inner temperature contour sliced at stagnation point. The  $(r, z) = (0, 0)$  point denotes the stagnation point. As the boiling heat transfer occurs at surface, the conduction heat transfer in depth direction occurs at the same time. The heat transfer rate going through the top surface is composed of complex interaction between the internal energy of surface and the conduction heat transfer from inside of specimen. Therefore, the thickness of specimen and thermal

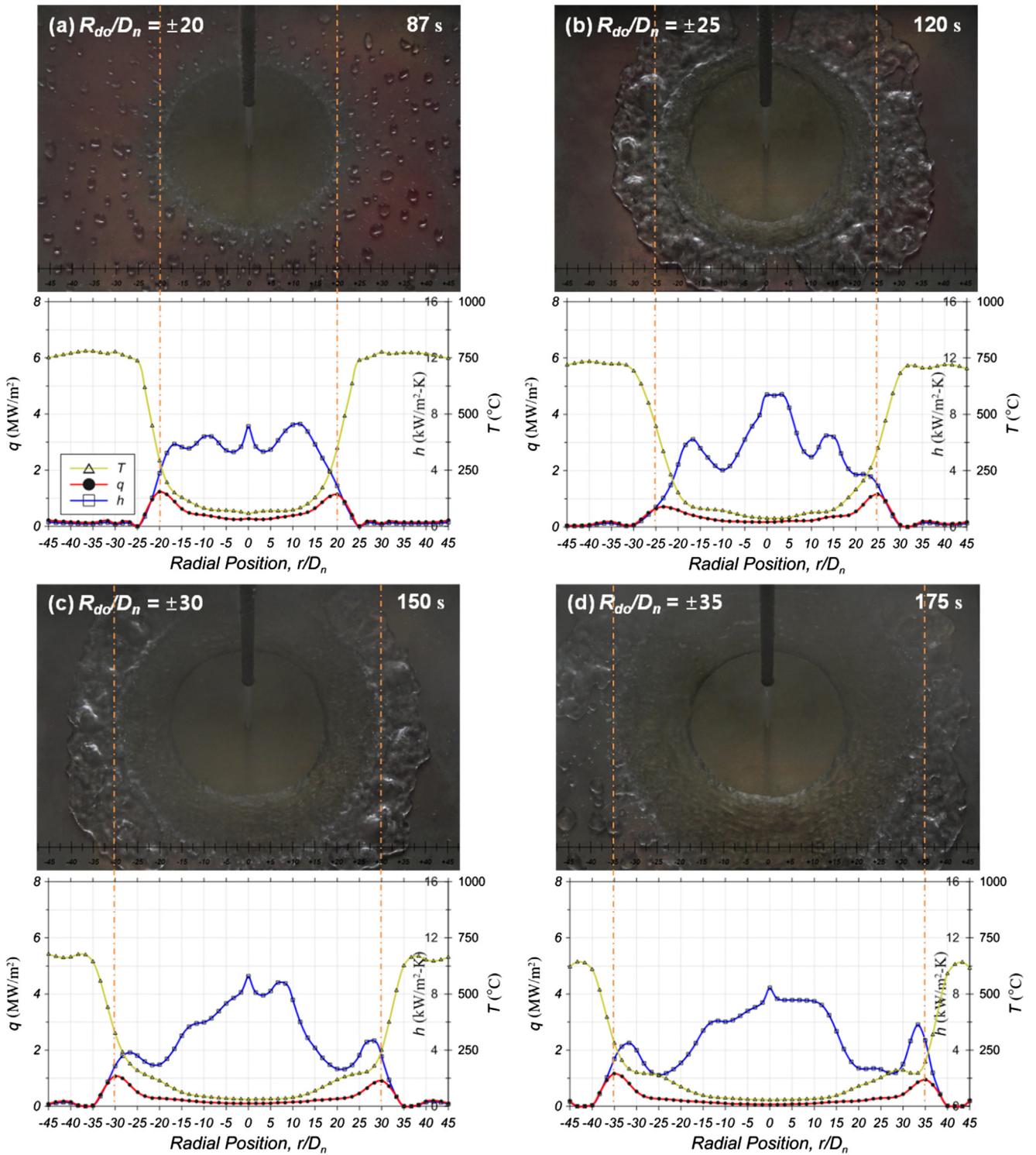
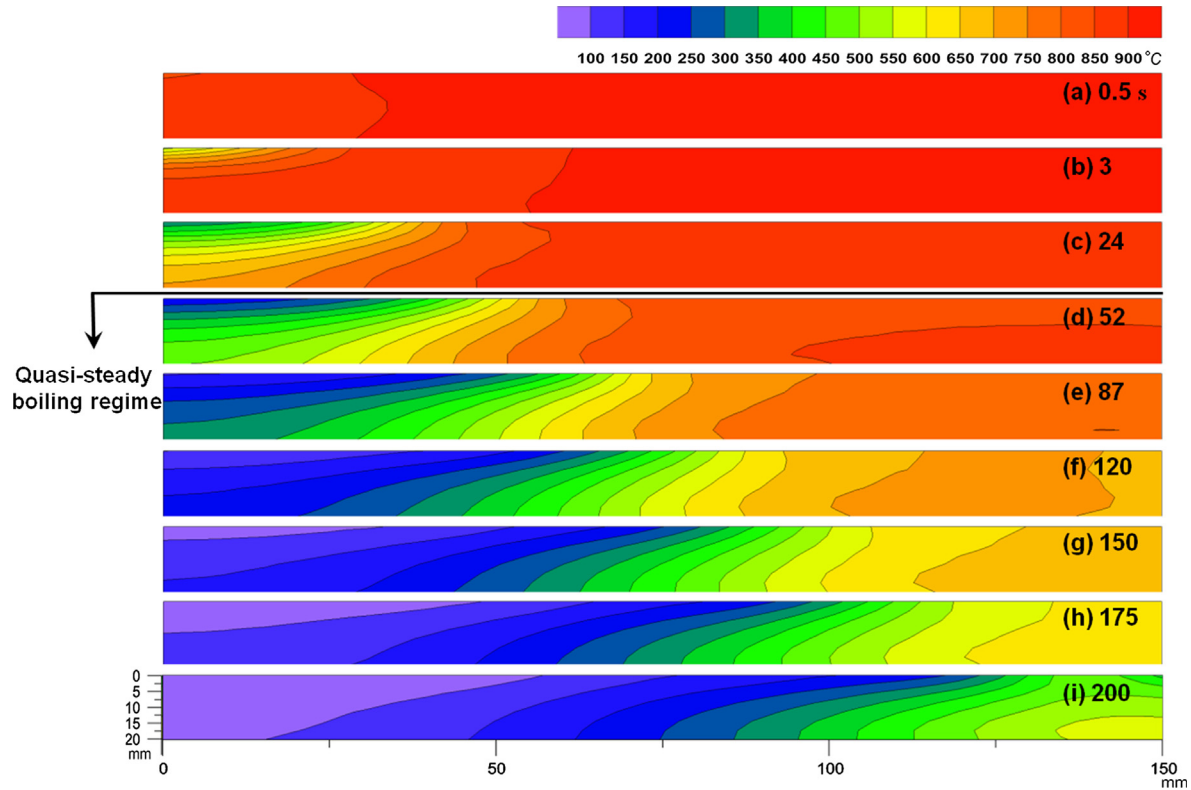


Fig. 11. Same as Fig. 10, but for  $R_{do}/D_n$  (a)  $\pm 20$ , (b)  $\pm 25$ , (c)  $\pm 30$ , and (d)  $\pm 35$ . The elapsed time is also chosen accordingly to reveal the regimes.

properties for conduction are deeply involved with the duration time of boiling heat transfer mode. As the thickness of specimen is thicker, the duration of each boiling mode can be longer. As shown in Fig. 12(c), the cooling of bottom surface starts in progress at 24 s. After that, the synchronization results of Figs. 10 and 11 show distinct quasi-steady characteristics like as the position of  $q_{max}$  and its value, and which time means the quasi-steady time ( $\tau_{qs}$ ).

### 3.3. Wetting front propagation

Fig. 13 shows the 3-D graph of surface heat transfer characteristic with surface heat flux, temperature and elapsed time. The difference of  $q_{max}$  at  $r/D_n = 0$  and 5 before the quasi-steady time shows larger value, but that of after the quasi-steady time shows very little change. This might be explained by two possible causes. First, the overall temperature of surface decreases as the time



**Fig. 12.** Variations of the inverse-conduction predicted temperature distribution within the plate at several elapsed times. The onset of the quasi-steady behavior is marked by the quasi-steady time reaching the back of the plate.

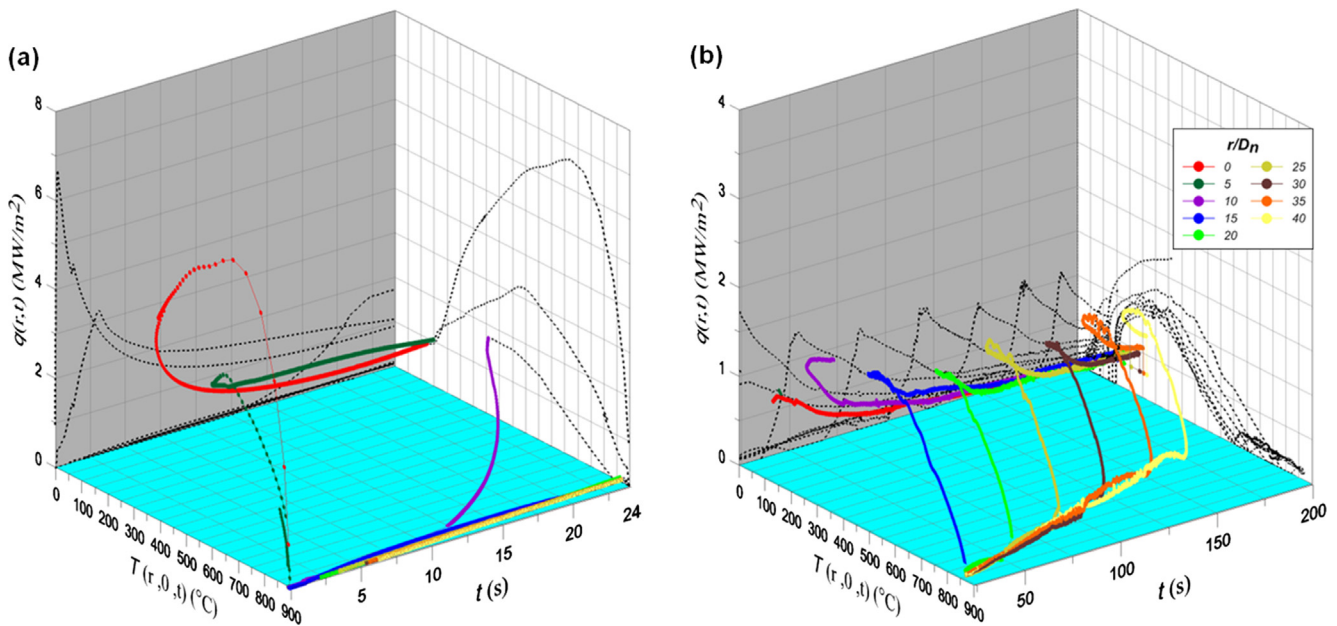


**Fig. 13.** Three-dimensional presentation of the simultaneous variations of the surface heat flux, surface temperature, and the elapsed time of (a) 0–24 (i.e.,  $\tau_{qs}$ ), and (b) 24–200 s, at several radial locations. The quasi-steady regime is noted with a similarity of the cooling behavior at various locations.

passes. The  $q_{\max}$  highly relates with the starting temperature of nucleate boiling. But the nucleate boiling at a radially outward position occurs at lower starting temperature as mentioned previous section. Second, the temperature gradient at outward position in depth direction becomes larger as time passes as shown in Fig. 12(d)–(i). The larger temperature gradient causes larger conduction heat transfer rate in depth direction. As a result, the low

starting temperature of nucleate boiling can lower the heat transfer rate, but the conduction heat transfer in depth direction is relatively high at the outward position. Therefore, the  $q_{\max}$  at several outward positions can be remained in similar value.

The quasi-steady regime is well presented in the graph of Fig. 14 which shows the radius of wetting front and position of  $q_{\max}$  against the elapsed time. In early stage before the quasi-

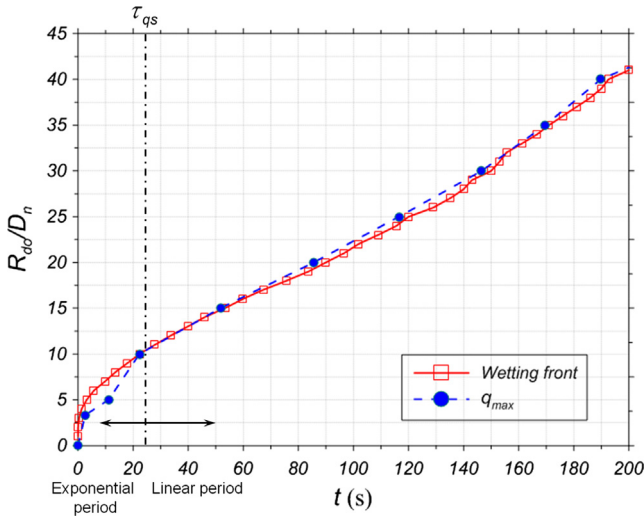


**Fig. 14.** Variation of the wetting front location with respect time, showing the quasi-steady regime where  $R_{0d}$  increases linearly with time. The position of the maximum heat flux at specific time is also marked.

steady time, the radius of wetting front shows exponential increase and the  $q_{max}$  occurs inside of wetted region. After the time  $\tau_{qs}$ , the both lines shows the linear increase and a good agreement between the radius of wetting front and position of  $q_{max}$ . These results are already visually and quantitatively verified in Figs. 10 and 11.

### 3.4. Fraction of liquid ejected at propagating front

In addition to the single-phase and subcooled boiling heat transfer, the droplets ejected at the front land on in the otherwise region and evaporate, resulting in significant cooling in that region. The fraction of liquid ejected is estimated as the evaporation fraction ( $\beta$ ). The local (discrete locations) surface heat flux  $\langle q \rangle_i$  from the axisymmetric inverse heat conduction analysis is used to obtain the total, instantaneous heat flow rate

$$Q = \sum_{i=1}^n \pi (R_{i+1}^2 - R_i^2) \langle q \rangle_i \quad (3)$$

where  $n$  is the number of surface segment sections and  $R_i$  is their radial locations from the center. The water jet flow is assumed to reach saturation temperature before ejection, so the fraction of liquid ejected and undergoing phase change can be expressed as the following equations,

$$\sum_{i=1}^n \pi (R_{i+1}^2 - R_i^2) \langle q \rangle_i = \beta \rho_l \pi \frac{D_n^2}{4} u_n \Delta h_{lg} \quad (4)$$

$$\therefore \beta = \frac{\sum_{i=1}^n \pi (R_{i+1}^2 - R_i^2) \langle q \rangle_i}{\rho_l \pi \frac{D_n^2}{4} u_n \Delta h_{lg}}$$

If we neglect evaporation at the wetting front, this would be the fraction of the ejected front (so it is rather overestimated). Fig. 15 (a) shows the fraction of liquid undergoing phase change  $\beta$  as a function of the elapse time. Once the quasi-steady state is reached  $\tau_{qs}$ , this fraction shows the linear shapes of graph. And the fraction of liquid  $\beta$  also shows the linear increase along the radial position and reaches over 10% of the liquid flowing out the nozzle as shown in Fig. 15(b). These ejected droplets land on the otherwise dry region and turn to be evaporated.

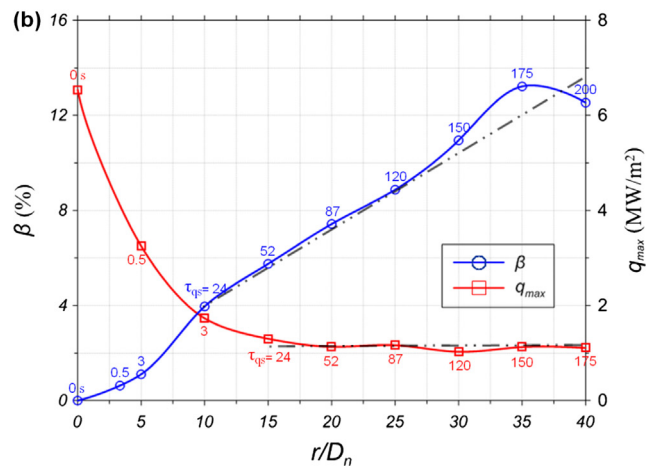
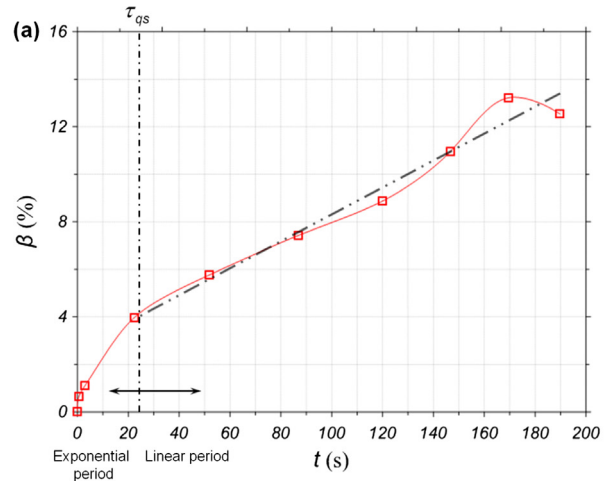


**Fig. 15.** (a) Variations of the fraction of liquid ejected at wetting front and evaporating as droplets in the dry region against the elapsed time and (b) variations of the fraction of liquid ejected at wetting front with the value of maximum heat flux along the radial position.

## 4. Conclusions

With high-resolution imaging and inverse heat conduction analysis we explore very high initial superheat and large surface area features of quench jet impingement boiling and explain the presence of (i) single-phase, (ii) collapsed-bubble (subcooled boiling), (iii) wetting front with ejecting droplets, and (iv) evaporating-droplets cooling regions on the plate. In the wetted region which covers the first three, the high heat flux is the largest. The wetting (or wet) front experiences violent nearly saturated nucleate boiling with high pressure bubbles erupting and causing ejection of droplets toward the dry region. The droplet-evaporation region is also very effective in cooling the plate. Heat conduction within the metallic plate is critical, with cooling spreading both laterally and through the plate. This is demonstrated through the 3-D graph of the measured surface heat flux and temperature at various radial locations versus time, and the predicted axisymmetric transient temperature distribution within the plate. A quasi-steady behavior prevails with the effect of thickness and thermal properties of specimen, where the radial wetting front location increases linearly with time. Liquid is ejected as droplets at the wetting front, and the analysis shows once the quasi-steady state is reached, the fraction of liquid ejected increases linearly with time and reaches over 10% of the liquid flowing out the nozzle. These ejected droplets land on the otherwise dry region and evaporate, which the evaporation rate depends on the local surface superheat at their

landing location. This evaporation cooling is very important in quench jet impingement cooling, as it substantially reduces the local surface temperature before the wetting front reaches it (i.e., precooling).

### Conflict of interest

The authors declare that there are no conflicts of interest.

### Acknowledgement

This work was supported by the Korea Institute of Energy Technology Evaluation and Planning (KETEP) grant funded by the Ministry of Trade, Industry & Energy, Korea (Grant No. 20142010102910) and the National Research Council of Science and Technology (NST) grant funded by the Ministry of Science, ICT and Future Planning, Korea (Grant No. KIMM-NK203B).

### References

- [1] S. Vakili, M.S. Gadala, Boiling heat transfer of multiple impinging jets on a hot moving plate, *Heat Transf. Eng.* 34 (2013) 580–595.
- [2] N. Karwa, L. Schmidt, P. Stephan, Hydrodynamics of quenching with impinging free-surface jet, *Int. J. Heat Mass Transf.* 55 (2012) 3677–3685.
- [3] T. Kim, D.-W. Oh, K.H. Do, J.M. Park, J. Lee, Effect of initial temperature of a cylindrical steel block on heat transfer characteristics of staggered array jets during water jet quenching, *Heat Transf. Eng.* 36 (2015) 1037–1045.
- [4] J. Lee, S. Sohn, J. Park, Visual observation of circular water jet impingement boiling on stationary hot steel plate, *J. Heat Transfer.* 137 (2015) 80911.
- [5] J. Lee, S. Sohn, S.G. Lee, Boiling visualization of two adjacent impinging jets on hot steel plate, *J. Heat Transfer.* 138 (2016) 20909.
- [6] D.H. Wolf, F.P. Incropera, R. Viskanta, Jet impingement boiling, *Adv. Heat Transfer.* 23 (1993) 1–132.
- [7] N. Karwa, T. Gambaryan-Roisman, P. Stephan, C. Tropea, Experimental investigation of circular free-surface jet impingement quenching: Transient hydrodynamics and heat transfer, *Exp. Therm. Fluid Sci.* 35 (2011) 1435–1443.
- [8] D.E. Hall, F.P. Incropera, R. Viskanta, Jet impingement boiling from a circular free-surface jet during quenching: Part 1—single-phase jet, *J. Heat Transfer.* 123 (2001) 901–910.
- [9] S. Ishigai, S. Nakanishi, T. Ochi, Boiling heat transfer for plane water jet impinging on a hot surface, in: *Proceedings of the Sixth International Heat Transfer Conference, Toronto, Ont., Canada, August 1978.*
- [10] P.L. Woodfield, M. Monde, A.K. Mozumder, Observations of high temperature impinging-jet boiling phenomena, *Int. J. Heat Mass Transf.* 48 (2005) 2032–2041.
- [11] H. Matsueda, M. Monde, S. Matsuda, Characteristics of transient heat transfer during quenching of a vertical hot surface with a falling liquid film, *Heat Transf. - Asian Res.* 36 (2007) 345–360.
- [12] M.A. Islam, M. Monde, P.L. Woodfield, Y. Mitsutake, Jet impingement quenching phenomena for hot surfaces well above the limiting temperature for solid-liquid contact, *Int. J. Heat Mass Transf.* 51 (2008) 1226–1237.
- [13] P.L. Woodfield, A.K. Mozumder, M. Monde, On the size of the boiling region in jet impingement quenching, *Int. J. Heat Mass Transf.* 52 (2009) 460–465.
- [14] M.N. Hasan, M. Monde, Y. Mitsutake, Homogeneous nucleation boiling during jet impingement quench of hot surfaces above thermodynamic limiting temperature, *Int. J. Heat Mass Transf.* 54 (2011) 2837–2843.
- [15] M. Zarringhalam, A. Karimipour, D. Toghraie, Experimental study of the effect of solid volume fraction and Reynolds number on heat transfer coefficient and pressure drop of CuO – Water nanofluid, *Exp. Therm. Fluid Sci.* 76 (2016) 342–351.
- [16] D. Toghraie, Numerical thermal analysis of water's boiling heat transfer based on a turbulent jet impingement on heated surface, *Phys. E Low-Dimensional Syst. Nanostruct.* 84 (2016) 454–465.
- [17] A.K. Mozumder, M. Monde, P.L. Woodfield, M.A. Islam, Maximum heat flux in relation to quenching of a high temperature surface with liquid jet impingement, *Int. J. Heat Mass Transf.* 49 (2006) 2877–2888.
- [18] J. Hammad, Y. Mitsutake, M. Monde, Movement of maximum heat flux and wetting front during quenching of hot cylindrical block, *Int. J. Therm. Sci.* 43 (2004) 743–752.
- [19] S. Tweomey, The application of numerical filtering for the solution of integral equations encountered in indirect sensing measurements, *J. Franklin Inst.* 279 (1965) 95–109.
- [20] J.V. Beak, B. Blackwell, C.R. St. Clair, *Inverse Heat Conduction*, Wiley, New York, NY, 1985.
- [21] M. Akmal, A.M.T. Omar, M.S. Hamed, Experimental investigation of propagation of wetting front on curved surfaces exposed to an impinging water jet, *Int. J. Microstruct. Mater. Prop.* 3 (4–5) (2008) 654–681.